Chapter 4

Theoretical Predictions for the CMB Bispectrum

In inflation, quantum fluctuations of scalar fields generate the matter and the radiation fluctuations in the universe (chapter 2). In the stochastic inflationary scenario of Starobinsky (1986), quantum fluctuations decohere to generate classical fluctuations. There are two potential sources of non-Gaussianity in this inflationary model: (a) non-linear coupling between the classical inflaton field and the observed fluctuation field, and (b) non-linear coupling between the quantum noise field and the classical fluctuation field. Salopek and Bond (1990, 1991) have studied the former; Gangui et al. (1994) have studied the latter.

Calzatta and Hu (1995) and Matacz (1997a,b) present an alternative treatment of the decoherence process that leads to different results for the primordial density perturbations from Starobinsky (1986). Matacz's treatment makes similar predictions for the level of non-Gaussianity to the Starobinsky's treatment (Matacz, 1997a,b). These studies conclude that in a slow-roll regime, fluctuations are Gaussian; however, features in a inflaton potential can produce significant non-Gaussianity (Kofman et al., 1991).

Previous work on the primary non-Gaussianity has focused on very large angular scales, the *COBE* scale, where the temperature fluctuations trace the primordial fluctuations. For *MAP* and *Planck*; however, we need the full effect of the radiation transfer function. In this chapter, we develop a formalism for doing this, and then present numerical results. Both the formalism and the numerical results are main results of this chapter. We also discuss how well we can separate the primary bispectrum from various secondary bispectra.

This chapter is organized as follows. In § 4.1, we define the angular bispectrum, the Gaunt integral, and a new quantity called the *reduced* bispectrum, which plays a fundamental role in estimating physical properties of the bispectrum. In § 4.2, we formulate the primary bispectrum that uses the full radiation transfer function, and presents numerical results for the primary bispectrum and skewness. In § 4.3, we calculate secondary bispectra from the coupling between the Sunyaev–Zel'dovich effect and the weak lensing effect (Spergel and Goldberg, 1999; Goldberg and Spergel, 1999; Cooray and Hu, 2000), and from extragalactic radio and infrared sources. In § 4.4, we study how well we can measure each bispectrum, and how well we can discriminate between those bispectra. § 4.5 is devoted to further discussion and our conclusions in this chapter.

4.1 Reduced Bispectrum

We expand the observed CMB temperature fluctuation field, $\Delta T(\hat{\mathbf{n}})/T$, into the spherical harmonics,

$$a_{lm} = \int d^2\hat{\mathbf{n}} \frac{\Delta T(\hat{\mathbf{n}})}{T} Y_{lm}^*(\hat{\mathbf{n}}), \tag{4.1}$$

where the hats denote unit vectors. The CMB angular bispectrum is given by

$$B_{l_1l_2l_3}^{m_1m_2m_3} \equiv \left\langle a_{l_1m_1}a_{l_2m_2}a_{l_3m_3}\right\rangle, \tag{4.2}$$

and the angular averaged bispectrum is (Eq.(3.18))

$$B_{l_1l_2l_3} = \sum_{\text{all } m} \begin{pmatrix} l_1 & l_2 & l_3 \\ m_1 & m_2 & m_3 \end{pmatrix} B_{l_1l_2l_3}^{m_1m_2m_3}, \tag{4.3}$$

where the matrix is the Wigner-$3j$ symbol. The bispectrum, $B_{l_1l_2l_3}^{m_1m_2m_3}$, satisfies the triangle conditions and parity invariance: $m_1+m_2+m_3=0$, $l_1+l_2+l_3=$ even, and $|l_i-l_j|\leq l_k \leq l_i+l_j$ for all permutations of indices. It implies that $B_{l_1l_2l_3}^{m_1m_2m_3}$ consists of the Gaunt integral, $\mathcal{G}_{l_1l_2l_3}^{m_1m_2m_3}$, defined by

$$\begin{aligned}
\mathcal{G}_{l_1l_2l_3}^{m_1m_2m_3} &\equiv \int d^2\hat{\mathbf{n}} Y_{l_1m_1}(\hat{\mathbf{n}})Y_{l_2m_2}(\hat{\mathbf{n}})Y_{l_3m_3}(\hat{\mathbf{n}}) \\
&= \sqrt{\frac{(2l_1+1)(2l_2+1)(2l_3+1)}{4\pi}} \begin{pmatrix} l_1 & l_2 & l_3 \\ 0 & 0 & 0 \end{pmatrix} \begin{pmatrix} l_1 & l_2 & l_3 \\ m_1 & m_2 & m_3 \end{pmatrix}.
\end{aligned} \tag{4.4}$$

$\mathcal{G}_{l_1l_2l_3}^{m_1m_2m_3}$ is real, and satisfies all the conditions mentioned above.

Rotational invariance of the angular three-point correlation function implies that $B_{l_1l_2l_3}$ is written as

$$B_{l_1l_2l_3}^{m_1m_2m_3} = \mathcal{G}_{l_1l_2l_3}^{m_1m_2m_3} b_{l_1l_2l_3}, \tag{4.5}$$

where $b_{l_1l_2l_3}$ is an arbitrary real symmetric function of l_1, l_2, and l_3. This form, equation (4.5), is necessary and sufficient to construct generic $B_{l_1l_2l_3}^{m_1m_2m_3}$ under rotational invariance; thus, we will use $b_{l_1l_2l_3}$ more frequently than $B_{l_1l_2l_3}^{m_1m_2m_3}$ in this chapter, and call this function the *reduced* bispectrum, as $b_{l_1l_2l_3}$ contains all physical information in $B_{l_1l_2l_3}^{m_1m_2m_3}$. Since the reduced bispectrum does not contain the Wigner-$3j$ symbol, which merely ensures the triangle conditions and parity invariance, it is easier to calculate physical properties of the bispectrum.

We calculate the angular averaged bispectrum, $B_{l_1l_2l_3}$, by substituting equation (4.5) into (4.3),

$$B_{l_1l_2l_3} = \sqrt{\frac{(2l_1+1)(2l_2+1)(2l_3+1)}{4\pi}} \begin{pmatrix} l_1 & l_2 & l_3 \\ 0 & 0 & 0 \end{pmatrix} b_{l_1l_2l_3}, \tag{4.6}$$

where we have used the identity,

$$\sum_{\text{all } m} \left(\begin{array}{ccc} l_1 & l_2 & l_3 \\ m_1 & m_2 & m_3 \end{array} \right) \mathcal{G}^{m_1 m_2 m_3}_{l_1 l_2 l_3} = \sqrt{\frac{(2l_1+1)(2l_2+1)(2l_3+1)}{4\pi}} \left(\begin{array}{ccc} l_1 & l_2 & l_3 \\ 0 & 0 & 0 \end{array} \right). \tag{4.7}$$

Alternatively, one can define the bispectrum in the flat-sky approximation,

$$\langle a(\mathbf{l}_1) a(\mathbf{l}_1) a(\mathbf{l}_3) \rangle = (2\pi)^2 \delta^{(2)} \left(\mathbf{l}_1 + \mathbf{l}_2 + \mathbf{l}_3 \right) B(\mathbf{l}_1, \mathbf{l}_2, \mathbf{l}_3), \tag{4.8}$$

where $\mathbf{l}$ is a two-dimensional wave vector on the sky. This definition of $B(\mathbf{l}_1, \mathbf{l}_2, \mathbf{l}_3)$ reduces to equation (4.5) with the correspondence, $\mathcal{G}^{m_1 m_2 m_3}_{l_1 l_2 l_3} \to (2\pi)^2 \delta^{(2)} \left(\mathbf{l}_1 + \mathbf{l}_2 + \mathbf{l}_3 \right)$, in the flat-sky limit (Hu, 2000). Thus, we have

$$b_{l_1 l_2 l_3} \approx B(\mathbf{l}_1, \mathbf{l}_2, \mathbf{l}_3) \qquad \text{(flat-sky approximation)}. \tag{4.9}$$

This fact motivates our using the reduced bispectrum, $b_{l_1 l_2 l_3}$, rather than the angular averaged bispectrum, $B_{l_1 l_2 l_3}$. Note that $b_{l_1 l_2 l_3}$ is similar to $\hat{B}_{l_1 l_2 l_3}$ defined by Magueijo (Magueijo, 2000); the relation is $b_{l_1 l_2 l_3} = \sqrt{4\pi} \hat{B}_{l_1 l_2 l_3}$.

4.2 Primary Bispectrum and Skewness

4.2.1 Model of the primordial non-Gaussianity

If primordial fluctuations are adiabatic scalar fluctuations, then

$$a_{lm} = 4\pi (-i)^l \int \frac{d^3\mathbf{k}}{(2\pi)^3} \Phi(\mathbf{k}) g_{\mathrm{T}l}(k) Y^*_{lm}(\hat{\mathbf{k}}), \tag{4.10}$$

where $\Phi(\mathbf{k})$ is the primordial curvature perturbation in Fourier space, and $g_{\mathrm{T}l}(k)$ is the radiation transfer function. a_{lm} takes over the non-Gaussianity, if any, from $\Phi(\mathbf{k})$. Although equation (4.10) is valid only if the universe is flat, it is straightforward to extend this to an arbitrary geometry. We can calculate the isocurvature fluctuations similarly by using the entropy perturbation and the proper transfer function.

In this chapter, we explore the simplest weak non-linear coupling case,

$$\Phi(\mathbf{x}) = \Phi_{\mathrm{L}}(\mathbf{x}) + f_{\mathrm{NL}} \left[\Phi^2_{\mathrm{L}}(\mathbf{x}) - \left\langle \Phi^2_{\mathrm{L}}(\mathbf{x}) \right\rangle \right], \tag{4.11}$$

in real space, where $\Phi_{\mathrm{L}}(\mathbf{x})$ denotes a linear Gaussian part of the perturbation, and $\langle \Phi(\mathbf{x}) \rangle = 0$ is guaranteed. Henceforth, we call f_{NL} the *non-linear coupling parameter*. This model is based upon slow-roll inflation; Salopek and Bond (1990, 1991) and Gangui et al. (1994) have found that f_{NL} is given by a certain combination of slope and curvature of an inflaton potential ($\Phi_3 = -2f_{\mathrm{NL}}$ in Gangui et al. (1994)). Gangui et al. (1994) have found that $|f_{\mathrm{NL}}| \sim 10^{-2}$ for quadratic and quartic potential models. We have reproduced these results in chapter 2.

In Fourier space, we decompose $\Phi(\mathbf{k})$ into two parts,

$$\Phi(\mathbf{k}) = \Phi_{\mathrm{L}}(\mathbf{k}) + \Phi_{\mathrm{NL}}(\mathbf{k}), \tag{4.12}$$

and accordingly we have

$$a_{lm} = a_{lm}^{\rm L} + a_{lm}^{\rm NL}, \tag{4.13}$$

where $\Phi_{\rm NL}(\mathbf{k})$ is a non-linear curvature perturbation defined by

$$\Phi_{\rm NL}(\mathbf{k}) \equiv f_{\rm NL}\left[\int \frac{d^3\mathbf{p}}{(2\pi)^3}\Phi_{\rm L}(\mathbf{k}+\mathbf{p})\Phi_{\rm L}^*(\mathbf{p}) - (2\pi)^3\delta^{(3)}(\mathbf{k})\left\langle \Phi_{\rm L}^2(\mathbf{x})\right\rangle\right]. \tag{4.14}$$

One can confirm that $\langle\Phi(\mathbf{k})\rangle = 0$ is satisfied. In this model, a non-vanishing component of the $\Phi(\mathbf{k})$-field bispectrum is

$$\langle\Phi_{\rm L}(\mathbf{k}_1)\Phi_{\rm L}(\mathbf{k}_2)\Phi_{\rm NL}(\mathbf{k}_3)\rangle = 2(2\pi)^3\delta^{(3)}(\mathbf{k}_1+\mathbf{k}_2+\mathbf{k}_3)f_{\rm NL}P_\Phi(k_1)P_\Phi(k_2), \tag{4.15}$$

where $P_\Phi(k)$ is the linear power spectrum given by

$$\langle\Phi_{\rm L}(\mathbf{k}_1)\Phi_{\rm L}(\mathbf{k}_2)\rangle = (2\pi)^3P_\Phi(k_1)\delta^{(3)}(\mathbf{k}_1+\mathbf{k}_2). \tag{4.16}$$

We have also used

$$\langle\Phi_{\rm L}(\mathbf{k}+\mathbf{p})\Phi_{\rm L}^*(\mathbf{p})\rangle = (2\pi)^3P_\Phi(p)\delta^{(3)}(\mathbf{k}), \tag{4.17}$$

and

$$\left\langle\Phi_{\rm L}^2(\mathbf{x})\right\rangle = (2\pi)^{-3}\int d^3\mathbf{k}P_\Phi(k). \tag{4.18}$$

Substituting equation (4.10) into (4.2), using equation (4.15) for the $\Phi(\mathbf{k})$-field bispectrum, and then integrating over angles $\hat{\mathbf{k}}_1$, $\hat{\mathbf{k}}_3$, and $\hat{\mathbf{k}}_3$, we obtain the primary CMB angular bispectrum,

$$\begin{aligned} B_{l_1l_2l_3}^{m_1m_2m_3} &= \left\langle a_{l_1m_1}^{\rm L}a_{l_2m_2}^{\rm L}a_{l_3m_3}^{\rm NL}\right\rangle + \left\langle a_{l_1m_1}^{\rm L}a_{l_2m_2}^{\rm NL}a_{l_3m_3}^{\rm L}\right\rangle + \left\langle a_{l_1m_1}^{\rm NL}a_{l_2m_2}^{\rm L}a_{l_3m_3}^{\rm L}\right\rangle \\ &= 2\mathcal{G}_{l_1l_2l_3}^{m_1m_2m_3}\int_0^\infty r^2dr\left[b_{l_1}^{\rm L}(r)b_{l_2}^{\rm L}(r)b_{l_3}^{\rm NL}(r) + b_{l_1}^{\rm L}(r)b_{l_2}^{\rm NL}(r)b_{l_3}^{\rm L}(r)\right. \\ &\quad \left. +b_{l_1}^{\rm NL}(r)b_{l_2}^{\rm L}(r)b_{l_3}^{\rm L}(r)\right], \end{aligned} \tag{4.19}$$

where

$$b_l^{\rm L}(r) \equiv \frac{2}{\pi}\int_0^\infty k^2dkP_\Phi(k)g_{{\rm T}l}(k)j_l(kr), \tag{4.20}$$

$$b_l^{\rm NL}(r) \equiv \frac{2}{\pi}\int_0^\infty k^2dkf_{\rm NL}g_{{\rm T}l}(k)j_l(kr). \tag{4.21}$$

Note that $b_l^{\rm L}(r)$ is dimensionless, while $b_l^{\rm NL}(r)$ has a dimension of L^{-3}.

One confirms that equation (4.5) holds; thus, the reduced bispectrum, $b_{l_1l_2l_3}$ (Eq.(4.5)), for the primordial non-Gaussianity is

$$\begin{aligned} b_{l_1l_2l_3}^{\rm primary} &= 2\int_0^\infty r^2dr\left[b_{l_1}^{\rm L}(r)b_{l_2}^{\rm L}(r)b_{l_3}^{\rm NL}(r) + b_{l_1}^{\rm L}(r)b_{l_2}^{\rm NL}(r)b_{l_3}^{\rm L}(r)\right. \\ &\quad \left. +b_{l_1}^{\rm NL}(r)b_{l_2}^{\rm L}(r)b_{l_3}^{\rm L}(r)\right]. \end{aligned} \tag{4.22}$$

We can fully specify $b_{l_1l_2l_3}^{\rm primary}$ by a single constant parameter, $f_{\rm NL}$, for the CMB angular power spectrum, C_l, will precisely measure cosmological parameters (Bond et al., 1997). We stress again that this is the special case in the slow-roll limit. If the slow-roll condition is not satisfied, then $f_{\rm NL} = f_{\rm NL}(k_1, k_2, k_3)$ at equation (4.15) (Gangui et al., 1994). Wang and Kamionkowski (2000) have developed a formula to compute $B_{l_1 l_2 l_3}$ from generic $\Phi(\mathbf{k})$-field bispectrum. Our formula (Eq.(4.19)) agrees with theirs, given our form of the $\Phi(\mathbf{k})$-field bispectrum (Eq.(4.15)).

Even if inflation produces Gaussian fluctuations, the general relativistic second-order perturbation theory produces $f_{\rm NL} \sim \mathcal{O}(1)$ (Pyne and Carroll, 1996). For generic slow-roll models, these terms dominate the primary non-Gaussianity.

4.2.2 Numerical results of the primary bispectrum

We calculate the primary CMB bispectrum (Eqs.(4.19)–(4.22)) numerically as follows. We compute the full radiation transfer function, $g_{{\rm T}l}(k)$, with the CMBFAST code (Seljak and Zaldarriaga, 1996), assuming a single power-law spectrum, $P_\Phi(k) \propto k^{n-4}$, for the primordial curvature fluctuations. After doing the integration over k (Eqs.(4.20) and (4.21)) with the same algorithm as of CMBFAST, we do the integration over r (Eq.(4.22)), $r = c\,(\tau_0 - \tau)$, where τ is the conformal time. τ_0 is the present-day value. In our model, $c\tau_0 = 11.8$ Gpc, and the decoupling occurs at $c\tau_* = 235$ Mpc at which the differential visibility has a maximum. Our $c\tau_0$ includes radiation effects on the expansion of the universe; otherwise, $c\tau_0 = 12.0$ Gpc. Since the most of the primary signal is generated at τ_*, we choose the r integration boundary as $c\,(\tau_0 - 2\tau_*) \le r \le c\,(\tau_0 - 0.1\tau_*)$. We use a step-size of $0.1c\tau_*$, as we have found that a step size of $0.01c\tau_*$ gives very similar results. As a cosmological model, we use the scale-invariant standard CDM model with $\Omega_{\rm m} = 1$, $\Omega_\Lambda = 0$, $\Omega_{\rm b} = 0.05$, $h = 0.5$, and $n = 1$, and with the power spectrum, $P_\Phi(k)$, normalized to *COBE* (Bunn and White, 1997). Although this model is almost excluded by current observations, it is still useful to depict basic effects of the transfer function on the bispectrum.

Figure 4.1 shows $b_l^{\rm L}(r)$ (Eq.(4.20)) and $b_l^{\rm NL}(r)$ (Eq.(4.21)) for several different values of r. We find that $b_l^{\rm L}(r)$ and C_l look very similar to each other in shape and amplitude at $l \gtrsim 100$, although the amplitude in the Sachs–Wolfe regime is different by a factor of -3. This is because $C_l \propto P_\Phi(k) g_{{\rm T}l}^2(k)$, while $b_l^{\rm L}(r) \propto P_\Phi(k) g_{{\rm T}l}(k)$, where $g_{{\rm T}l} = -1/3$. We also find that $b_l^{\rm L}(r)$ has a good phase coherence over wide range of r, while the phase of $b_l^{\rm NL}(r)$ in the high-l regime oscillates rapidly as a function of r. This strongly damps the integrated result (Eq.(4.19)) in the high-l regime. The main difference between C_l and $b_l(r)$ is that $b_l(r)$ changes the sign, while C_l does not.

Looking at figure 4.1, we find $l^2 b_l^{\rm L} \sim 2 \times 10^{-9}$ and $b_l^{\rm NL} f_{\rm NL}^{-1} \sim 10^{-10}$ Mpc^{-3}. The most signal coming from the decoupling, the volume element at τ_* is $r_*^2 \Delta r_* \sim (10^4)^2 \times 10^2$ Mpc^3; thus, we estimate an order of magnitude of the primary reduced bispectrum (Eq.(4.22)) as

$$b_{lll}^{\rm primary} \sim l^{-4} \left[2 r_*^2 \Delta r_* \left(l^2 b_l^{\rm L} \right)^2 b_l^{\rm NL} \times 3 \right] \sim l^{-4} \times 2 \times 10^{-17} f_{\rm NL}. \tag{4.23}$$

Since $b_l^{\rm NL} f_{\rm NL}^{-1} \sim r_*^{-2} \delta(r - r_*)$ (see Eq.(4.26)), $r_*^2 \Delta r_* b_l^{\rm NL} f_{\rm NL}^{-1} \sim 1$. This rough estimate agrees with the numerical result below (figure 4.2).

Figure 4.2 shows the integrated bispectrum (Eq.(4.19)) divided by the Gaunt integral, $\mathcal{G}_{l_1 l_2 l_3}^{m_1 m_2 m_3}$, which is the reduced bispectrum, $b_{l_1 l_2 l_3}^{\rm primary}$. While the bispectrum is a 3-d function, we show different

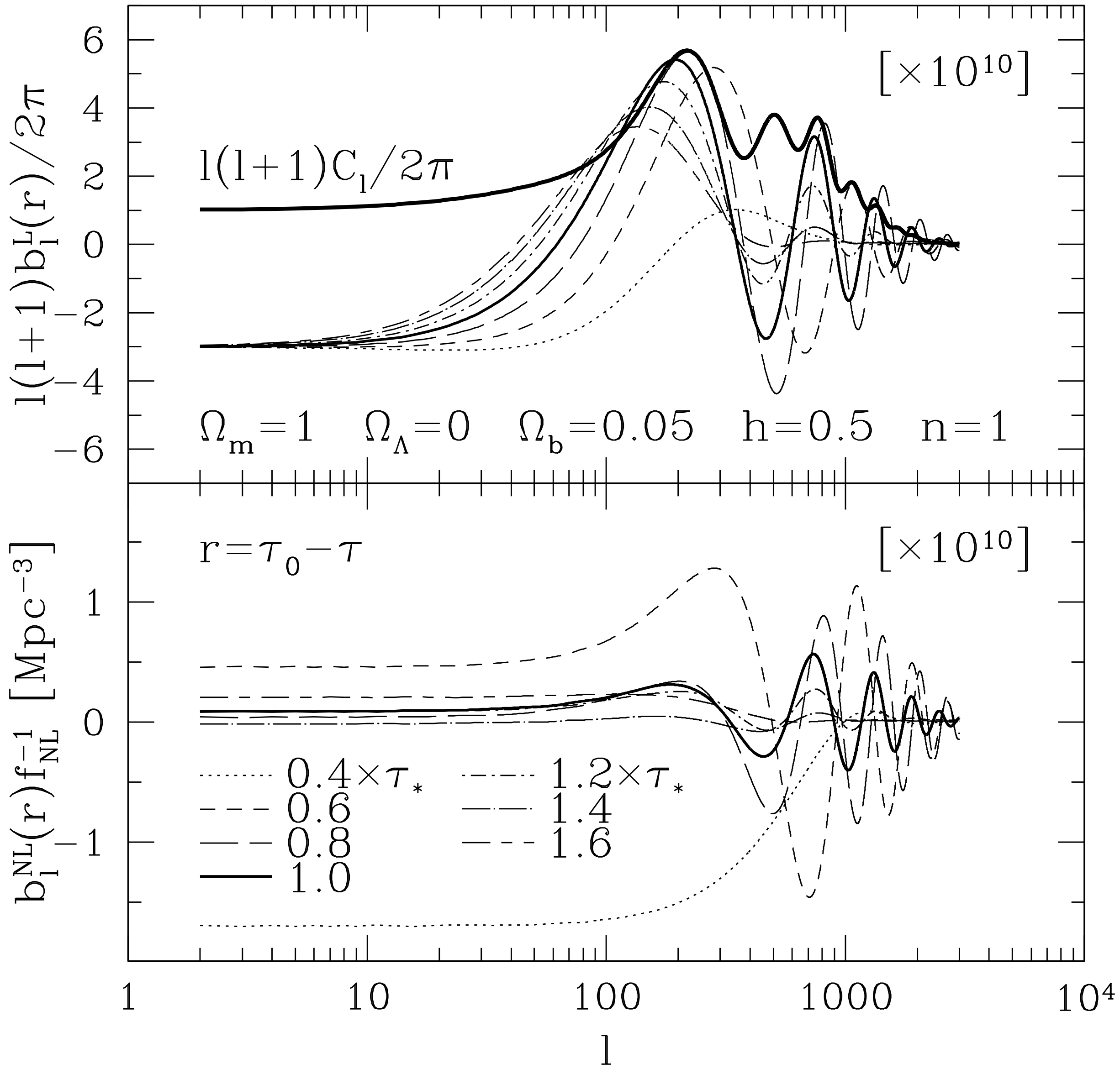

Figure 4.1: Components of Primary CMB Bispectrum

This figure shows $b^{\rm L}_l(r)$ (Eq.(4.20)) and $b^{\rm NL}_l(r)$ (Eq.(4.21)), the two terms in our calculation of the primary CMB angular bispectrum, as a function of r. Various lines in the top panel show $\left[l(l+1)b^{\rm L}_l(r)/2\pi\right] \times 10^{10}$, where $r = c\,(\tau_0 - \tau)$, at $\tau = 0.4, 0.6, 0.8, 1.0, 1.2, 1.4,$ and $1.6 \times \tau_*$ (decoupling time); $\left[b^{\rm NL}_l(r)f^{-1}_{\rm NL}\right] \times 10^{10}$ are shown in the bottom panel. τ_0 is the present-day conformal time. Note that $c\tau_0 = 11.8$ Gpc, and $c\tau_* = 235$ Mpc in our cosmological model chosen here. The thickest solid line in the top panel is the CMB angular power spectrum, $[l(l+1)C_l/2\pi] \times 10^{10}$. C_l is shown for comparison.

1-d slices of the bispectrum in this figure. We plot

$$l_2(l_2+1)l_3(l_3+1)\left\langle a^{\rm NL}_{l_1m_1}a^{\rm L}_{l_2m_2}a^{\rm L}_{l_3m_3}\right\rangle\left(\mathcal{G}^{m_1m_2m_3}_{l_1l_2l_3}\right)^{-1}/(2\pi)^2$$

as a function of l_3 in the top panel, while we plot

$$l_1(l_1+1)l_2(l_2+1)\left\langle a^{\rm L}_{l_1m_1}a^{\rm L}_{l_2m_2}a^{\rm NL}_{l_3m_3}\right\rangle\left(\mathcal{G}^{m_1m_2m_3}_{l_1l_2l_3}\right)^{-1}/(2\pi)^2$$

in the bottom panel. We have multiplied each $b^{\rm L}_l(r)$ which contains $P_\Phi(k)$ by $l(l+1)/(2\pi)$ so that the Sachs–Wolfe plateau at $l_3 \lesssim 10$ is easily seen. We have chosen l_1 and l_2 so as $(l_1,l_2)=(9,11),(99,101),(199,201)$, and $(499,501)$. We find that the $(l_1,l_2)=(199,201)$ mode, the first acoustic peak mode, has the largest signal in this family of parameters. The top panel has a prominent first acoustic peak, and strongly damped oscillations in the high-l regime; the bottom panel also has a first peak, but damps more slowly. Typical amplitude of the reduced bispectrum is $l^4 b^{\rm primary}_{lll} f^{-1}_{\rm NL} \sim 10^{-17}$, which agrees with an order of magnitude estimate (Eq.(4.23)).

Our formula (Eq.(4.22)) and numerical results agree with Gangui et al. (1994) in the Sachs–Wolfe regime, where $g_{{\rm T}l}(k)\approx -j_l(kr_*)/3$, and

$$b^{\rm primary}_{l_1l_2l_3} \approx -6f_{\rm NL}\left(C^{\rm SW}_{l_1}C^{\rm SW}_{l_2}+C^{\rm SW}_{l_1}C^{\rm SW}_{l_3}+C^{\rm SW}_{l_2}C^{\rm SW}_{l_3}\right) \qquad \text{(SW approximation)}. \tag{4.24}$$

Each term is in the same order as equation (4.22). Here, $C^{\rm SW}_l$ is the CMB angular power spectrum in the Sachs–Wolfe approximation,

$$C^{\rm SW}_l \equiv \frac{2}{9\pi}\int_0^\infty k^2 dk P_\Phi(k) j^2_l(kr_*). \tag{4.25}$$

In deriving equation (4.24) from (4.22), we have approximated $b^{\rm NL}_l(r)$ (Eq.(4.21)) with

$$b^{\rm NL}_l(r) \approx \left(-\frac{f_{\rm NL}}{3}\right)\frac{2}{\pi}\int_0^\infty k^2 dk j_l(kr_*)j_l(kr) = -\frac{f_{\rm NL}}{3}r_*^{-2}\delta(r-r_*). \tag{4.26}$$

The Sachs–Wolfe approximation (Eq.(4.24)) is valid only when l_1, l_2, and l_3 are all smaller than $\sim$ 10, for which Gangui et al. (1994) gives $\sim -6\times 10^{-20}$ in figure 4.2. We stress again that the Sachs–Wolfe approximation gives a qualitatively different result from our full calculation (Eq.(4.22)) at $l_i \gtrsim 10$. The full bispectrum does change the sign; the approximation never changes the sign because of using $C^{\rm SW}_l$. The acoustic oscillation and the sign change are actually great advantages, when we try to separate the primary bispectrum from various secondary bispectra. We will study this point later.

4.2.3 Primary skewness

The skewness, S_3, given by

$$S_3 \equiv \left\langle \left(\frac{\Delta T(\hat{\mathbf{n}})}{T}\right)^3 \right\rangle, \tag{4.27}$$

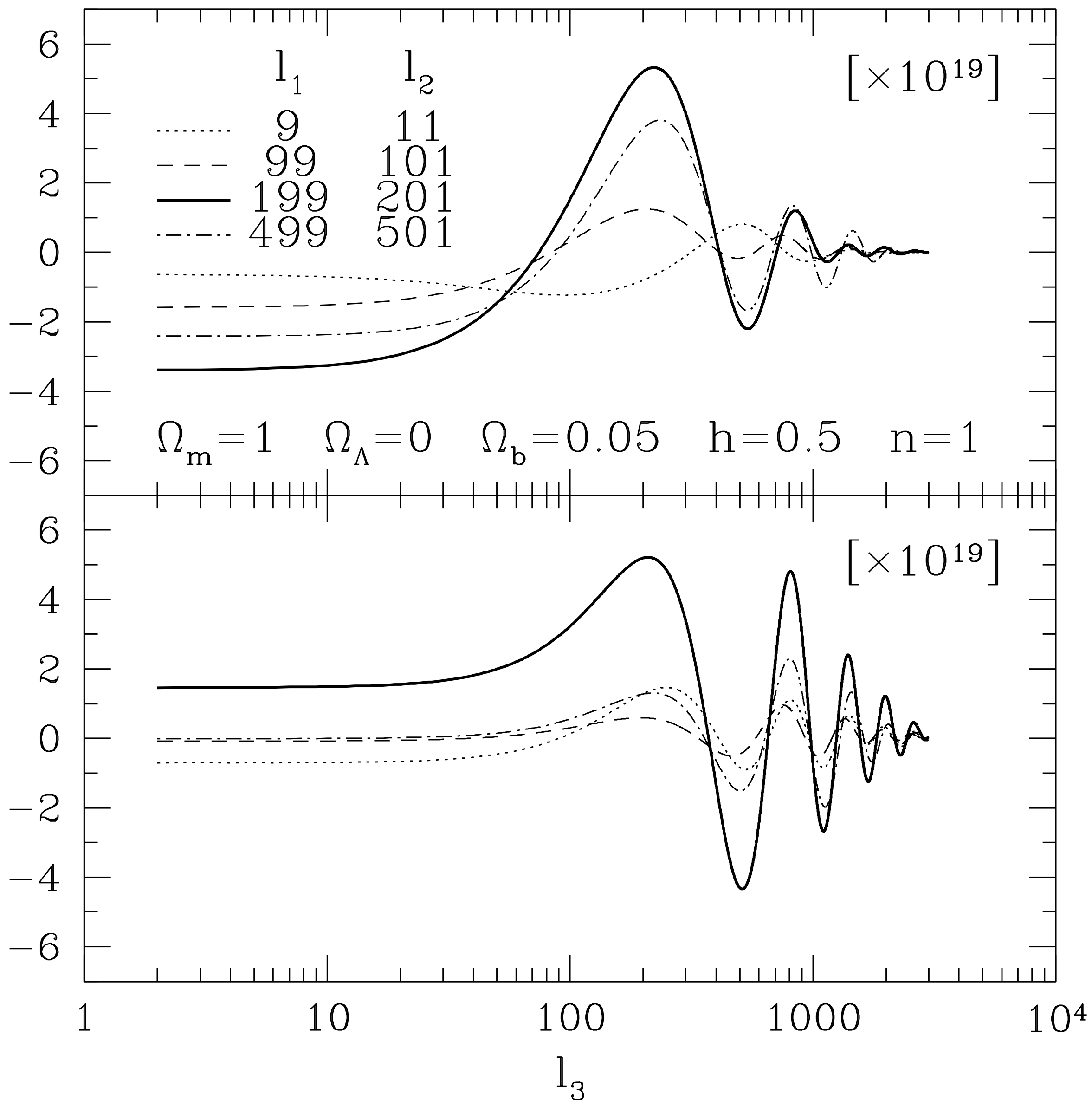

Figure 4.2: Primary CMB Bispectrum

The primary angular bispectrum (Eq.(4.19)), divided by the Gaunt integral, $\mathcal{G}^{m_1m_2m_3}_{l_1l_2l_3}$ (Eq.(4.4)). The bispectrum is plotted as a function of l_3 for (l_1, l_2) =(9,11), (99,101), (199,201), and (499,501). Each panel plots a different 1-dimensional slice of the bispectrum. The top panel plots $l_2(l_2+1)l_3(l_3+1)\left\langle a^{\rm NL}_{l_1m_1}a^{\rm L}_{l_2m_2}a^{\rm L}_{l_3m_3}\right\rangle f^{-1}_{\rm NL}\left(\mathcal{G}^{m_1m_2m_3}_{l_1l_2l_3}\right)^{-1}/(2\pi)^2$, while the bottom panel plots $l_1(l_1+1)l_2(l_2+1)\left\langle a^{\rm L}_{l_1m_1}a^{\rm L}_{l_2m_2}a^{\rm NL}_{l_3m_3}\right\rangle f^{-1}_{\rm NL}\left(\mathcal{G}^{m_1m_2m_3}_{l_1l_2l_3}\right)^{-1}/(2\pi)^2$. Note that we have multiplied the bispectrum in each panel by a factor of 10^{19}.

is the simplest statistic characterizing non-Gaussianity. We expand S_3 in terms of $B_{l_1l_2l_3}$ (Eq.(4.3)), or $b_{l_1l_2l_3}$ (Eq.(4.5)), as

$$\begin{aligned} S_3 &= \frac{1}{4\pi}\sum_{l_1l_2l_3}\sqrt{\frac{(2l_1+1)(2l_2+1)(2l_3+1)}{4\pi}}\left(\begin{array}{ccc} l_1 & l_2 & l_3 \\ 0 & 0 & 0 \end{array}\right) B_{l_1l_2l_3}W_{l_1}W_{l_2}W_{l_3} \\ &= \frac{1}{2\pi^2}\sum_{2\leq l_1l_2l_3}\left(l_1+\frac{1}{2}\right)\left(l_2+\frac{1}{2}\right)\left(l_3+\frac{1}{2}\right)\left(\begin{array}{ccc} l_1 & l_2 & l_3 \\ 0 & 0 & 0 \end{array}\right)^2 \\ &\quad \times b_{l_1l_2l_3}W_{l_1}W_{l_2}W_{l_3}, \end{aligned} \tag{4.28}$$

where W_l is the experimental window function. We have used equation (4.6) to replace $B_{l_1l_2l_3}$ by the reduced bispectrum, $b_{l_1l_2l_3}$, in the last equality. Since $l=0$ and 1 modes are not observable, we have excluded them from the summation. Throughout this chapter, we consider a single-beam window function, $W_l = e^{-l(l+1)/(2\sigma_{\rm b}^2)}$, where $\sigma_{\rm b} = {\rm FWHM}/\sqrt{8\ln 2}$. Since $\left(\begin{array}{ccc} l_1 & l_2 & l_3 \\ 0 & 0 & 0 \end{array}\right)^2 b_{l_1l_2l_3}$ is symmetric under permutation of indices, we change the way of summation as

$$\sum_{2\leq l_1l_2l_3} \longrightarrow 6\sum_{2\leq l_1\leq l_2\leq l_3}. \tag{4.29}$$

This reduces the number of summations by a factor of $\simeq 6$. We will use this convention henceforth.

The top panel of figure 4.3 plots $S_3(<l_3)$, which is S_3 summed up to a certain l_3, for FWHM beam sizes of 7°, $13'$, and $5'\!.5$. These values correspond to *COBE*, *MAP*, and *Planck* beam sizes, respectively. Figure 4.3 also plots the infinitesimally thin beam case. We find that *MAP*, *Planck*, and the ideal experiments measure very similar S_3 to one another, despite the fact that *Planck* and the ideal experiments can use much more number of modes than *MAP*. The reason is as follows. Looking at equation (4.28), one finds that S_3 is a linear integral of $b_{l_1l_2l_3}$ over l_i; thus, integrating oscillations in $b^{\rm primary}_{l_1l_2l_3}$ around zero (see figure 4.2) damps the non-Gaussian signal on small angular scales, $l \gtrsim 300$. Since the Sachs–Wolfe effect, no oscillation, dominates the *COBE* scale anisotropy, the cancellation on the *COBE* scales affects S_3 less significantly than on the *MAP* and *Planck* scales. *Planck* suffers from severe cancellation in small angular scales: *Planck* and the ideal experiments measure only the same amount of S_3 as *MAP* does. As a result, measured S_3 almost saturates at the *MAP* resolution scale, $l \sim 500$.

We conclude this section by noting that when we can calculate the expected form of the bispectrum, then it becomes a "matched filter" for detecting the non-Gaussianity in data, and thus much more powerful tool than the skewness in which the information is lost through the coarse-graining.

4.3 Secondary Sources of the CMB Bispectrum

Even if the CMB bispectrum were significantly detected in the CMB map, the origin would not necessarily be primordial, but rather would be various secondary sources such as the Sunyaev–Zel'dovich (SZ) effect (Zel'dovich and Sunyaev, 1969), the weak lensing effect, and so on, or fore-

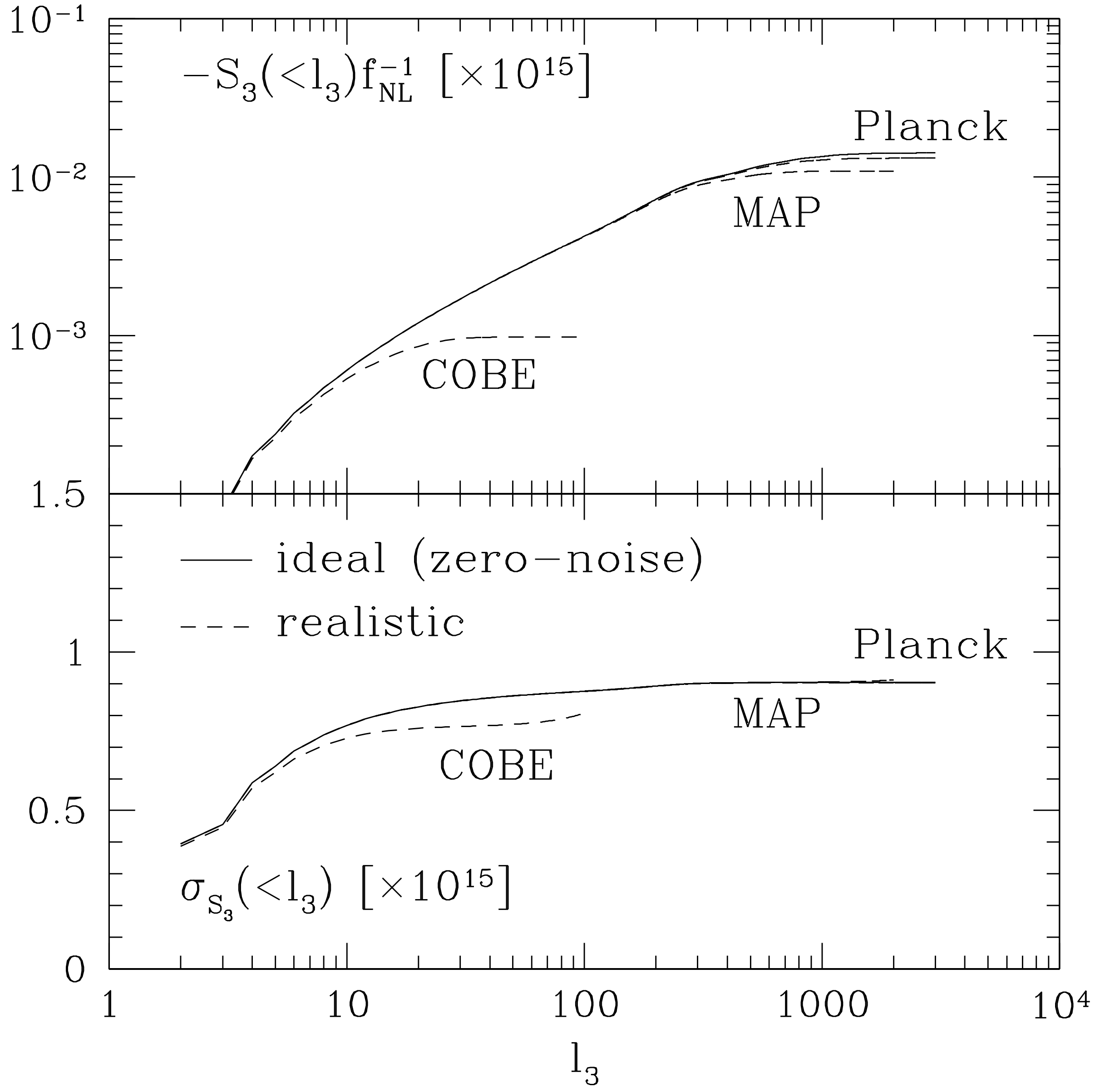

Figure 4.3: Primary Skewness

The top panel shows the primary CMB skewness (Eq.(4.28)) summed up to a certain l_3, $-S_3(< l_3)f_{\rm NL}^{-1} \times 10^{15}$. The bottom panel shows the error of S_3 (Eq.(4.63)) summed up to l_3, $\sigma_{S_3}(< l_3) \times 10^{15}$. The solid line represents the zero-noise ideal experiment, while the dotted lines show *COBE*, *MAP*, and *Planck* experiments.

ground sources such as extragalactic radio sources. To isolate the primordial origin from the others, we have to know the accurate form of bispectra produced by secondary and foreground sources.

4.3.1 Coupling between the weak lensing and the Sunyaev–Zel'dovich effects

The coupling between the SZ effect and the weak lensing effect produces an observable effect in the bispectrum (Goldberg and Spergel, 1999; Cooray and Hu, 2000). We expand the CMB temperature field including the SZ and the lensing effect as

$$\begin{aligned}\frac{\Delta T(\hat{\mathbf{n}})}{T} &= \frac{\Delta T^{\mathrm{P}}\left(\hat{\mathbf{n}}+\nabla\Theta(\hat{\mathbf{n}})\right)}{T}+\frac{\Delta T^{\mathrm{SZ}}(\hat{\mathbf{n}})}{T}\\ &\approx \frac{\Delta T^{\mathrm{P}}(\hat{\mathbf{n}})}{T}+\nabla\left(\frac{\Delta T^{\mathrm{P}}(\hat{\mathbf{n}})}{T}\right)\cdot\nabla\Theta(\hat{\mathbf{n}})+\frac{\Delta T^{\mathrm{SZ}}(\hat{\mathbf{n}})}{T},\end{aligned} \tag{4.30}$$

where P denotes the primary anisotropy, $\Theta(\hat{\mathbf{n}})$ is the lensing potential,

$$\Theta(\hat{\mathbf{n}}) \equiv -2\int_0^{r_*} dr\frac{r_*-r}{rr_*}\Phi(r,\hat{\mathbf{n}}r), \tag{4.31}$$

and SZ denotes the SZ effect,

$$\frac{\Delta T^{\mathrm{SZ}}(\hat{\mathbf{n}})}{T} = y(\hat{\mathbf{n}})j_\nu, \tag{4.32}$$

where j_ν is a spectral function of the SZ effect (Zel'dovich and Sunyaev, 1969). $y(\hat{\mathbf{n}})$ is the Compton y-parameter given by

$$y(\hat{\mathbf{n}}) \equiv y_0\int\frac{dr}{r_*}\frac{T_\rho(r,\hat{\mathbf{n}}r)}{\overline{T}_{\rho 0}}a^{-2}(r), \tag{4.33}$$

where

$$y_0 \equiv \frac{\sigma_T\overline{\rho}_{\mathrm{gas}0}k_{\mathrm{B}}\overline{T}_{\rho 0}r_*}{\mu_e m_p m_e c^2} = 4.3\times 10^{-4}\mu_e^{-1}\left(\Omega_{\mathrm{b}}h^2\right)\left(\frac{k_{\mathrm{B}}\overline{T}_{\rho 0}}{1\text{ keV}}\right)\left(\frac{r_*}{10\text{ Gpc}}\right). \tag{4.34}$$

$T_\rho \equiv \rho_{\mathrm{gas}}T_e/\overline{\rho}_{\mathrm{gas}}$ is the electron temperature weighted by the gas mass density, the overline denotes the volume average, and the subscript 0 means the present epoch. We adopt $\mu_e^{-1} = 0.88$, where $\mu_e^{-1} \equiv n_e/(\rho_{\mathrm{gas}}/m_p)$ is the number of electrons per proton mass in the fully ionized medium. Other quantities have their usual meanings.

Transforming equation (4.30) into harmonic space, we obtain

$$\begin{aligned}a_{lm} &= a_{lm}^{\mathrm{P}}+\sum_{l'm'}\sum_{l''m''}(-1)^m\mathcal{G}_{ll'l''}^{-mm'm''}\\ &\quad\times\frac{l'(l'+1)-l(l+1)+l''(l''+1)}{2}a_{l'm'}^{\mathrm{P}}\Theta_{l''m''}+a_{lm}^{\mathrm{SZ}}\\ &= a_{lm}^{\mathrm{P}}+\sum_{l'm'}\sum_{l''m''}(-1)^{m+m'+m''}\mathcal{G}_{ll'l''}^{-mm'm''}\\ &\quad\times\frac{l'(l'+1)-l(l+1)+l''(l''+1)}{2}a_{l'-m'}^{P*}\Theta_{l''-m''}^{*}+a_{lm}^{\mathrm{SZ}},\end{aligned} \tag{4.35}$$

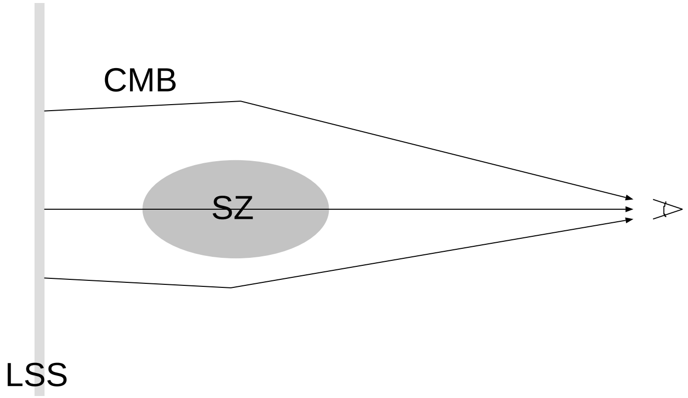

Figure 4.4: SZ–lensing Coupling

A schematic view of the SZ–lensing coupling bispectrum. One of the three CMB photons, which are decoupled at the last scattering surface (LSS), penetrates through a SZ cluster, changing its temperature, and coming toward us. As the other two photons pass through near the SZ cluster, they are deflected by the lensing effect, changing their propagation directions, and coming toward us. As a result, the three photons are correlated, generating three-point correlation, the bispectrum.

where $\mathcal{G}_{l_1 l_2 l_3}^{m_1 m_2 m_3}$ is the Gaunt integral (Eq.(4.4)). Substituting equation (4.35) into (4.2), and using the identity, $\mathcal{G}_{l_1 l_2 l_3}^{-m_1 -m_2 -m_3} = \mathcal{G}_{l_1 l_2 l_3}^{m_1 m_2 m_3}$, we obtain the bispectrum,

$$\begin{aligned} B_{l_1 l_2 l_3}^{m_1 m_2 m_3} &= \mathcal{G}_{l_1 l_2 l_3}^{m_1 m_2 m_3} \left[\frac{l_1(l_1+1) - l_2(l_2+1) + l_3(l_3+1)}{2} C_{l_1}^{\mathrm{P}} \left\langle \Theta_{l_3 m_3}^* a_{l_3 m_3}^{\mathrm{SZ}} \right\rangle \right. \\ & \left. +5 \text{ permutations} \right]. \end{aligned} \tag{4.36}$$

The form of equation (4.5) is confirmed; the reduced bispectrum $b_{l_1 l_2 l_3}^{\mathrm{sz-lens}}$ includes the terms in the square bracket.

While equation (4.36) is complicated, we can understand the physical effect producing the SZ–lensing bispectrum intuitively. Figure 4.4 shows how the SZ–lensing coupling produces the three-point correlation. Suppose that there are three CMB photons decoupled at the last scattering surface (LSS), and one of these photons penetrates through a SZ cluster between LSS and us; the energy of the photon changes because of the SZ effect. When the other two photons pass through near the SZ cluster, they are deflected by the gravitational lensing effect, changing their propagation directions, and coming toward us. What do we see after all? We see that the three CMB photons are correlated; we measure non-zero angular bispectrum. The cross-correlation strength between the SZ and lensing effects, $\left\langle \Theta_{l_3 m_3}^* a_{l_3 m_3}^{\mathrm{SZ}} \right\rangle$, thus determines the bispectrum amplitude, as indicated by equation (4.36).

Goldberg and Spergel (1999) have derived $\left\langle \Theta_{lm}^* a_{lm}^{\mathrm{SZ}} \right\rangle$, assuming the linear pressure bias model (Persi et al., 1995), $T_\rho = \overline{T}_\rho b_{\mathrm{gas}} \delta$, and the mean temperature evolution, $\overline{T}_\rho \simeq \overline{T}_{\rho 0}(1+z)^{-1}$, for $z < 2$, which is roughly suggested by recent hydrodynamic simulations (Cen and Ostriker, 1999;

Refregier et al., 2000; Springel et al., 2001). They have obtained

$$\left\langle \Theta^*_{lm} a^{\rm SZ}_{lm} \right\rangle \simeq -j_\nu \frac{4y_0 b_{\rm gas} l^2}{3\Omega_{\rm m} H_0^2} \int_0^{z_*} dz \frac{dr}{dz} D^2(z)(1+z)^2 \frac{r_* - r(z)}{r_*^2 r^5(z)} P_\Phi\left(k = \frac{l}{r(z)}\right), \tag{4.37}$$

where $D(z)$ is the linear growth factor. Simulations without non-gravitational heating (Refregier et al., 2000; Springel et al., 2001) suggest that $\overline{T}_{\rho 0} \sim 0.2 - 0.4$ keV and $b_{\rm gas} \sim 5 - 10$; analytic estimations give similar numbers (Refregier et al., 2000; Zhang and Pen, 2001). In the pressure bias model, free parameters except cosmological parameters are $\overline{T}_{\rho 0}$ and $b_{\rm gas}$; however, both actually depend upon cosmological models (Refregier et al., 2000). Since $l^3 \left\langle \Theta^*_{lm} a^{\rm SZ}_{lm} \right\rangle \sim 2 \times 10^{-10} j_\nu \overline{T}_{\rho 0} b_{\rm gas}$ (Goldberg and Spergel, 1999; Cooray and Hu, 2000) and $l^2 C_l^{\rm P} \sim 6 \times 10^{-10}$, we have

$$b^{\rm sz-lens}_{lll} \sim l^{-3} \left[\left(l^2 C_l^{\rm P}\right) \left(l^3 \left\langle \Theta^*_{lm} a^{\rm SZ}_{lm} \right\rangle\right) \times 5/2 \right] \sim l^{-3} \times 3 \times 10^{-19} j_\nu \overline{T}_{\rho 0} b_{\rm gas}, \tag{4.38}$$

where $\overline{T}_{\rho 0}$ is in units of 1 keV, and $b_{l_1 l_2 l_3} = B^{m_1 m_2 m_3}_{l_1 l_2 l_3} \left(\mathcal{G}^{m_1 m_2 m_3}_{l_1 l_2 l_3}\right)^{-1}$ is the reduced bispectrum (Eq.(4.5)). Comparing this with equation (4.23), we obtain

$$\frac{b^{\rm primary}_{lll}}{b^{\rm sz-lens}_{lll}} \sim l^{-1} \times 10 \left(\frac{f_{\rm NL}}{j_\nu \overline{T}_{\rho 0} b_{\rm gas}} \right). \tag{4.39}$$

This estimate suggests that the SZ–lensing bispectrum overwhelms the primary bispectrum in small angular scales. This is why we have to separate the primary from the SZ–lensing effect.

While the pressure bias model gives a rough estimate of the SZ power spectrum, more accurate predictions exist. Several authors have predicted the SZ power spectrum analytically using the Press-Schechter approach (Cole and Kaiser, 1988; Makino and Suto, 1993; Atrio-Barandela and Mücket, 1999; Komatsu and Kitayama, 1999; Cooray, 2000) or the hyper-extended perturbation theory (Zhang and Pen, 2001). The predictions agree with hydrodynamic simulations well (Refregier et al., 2000; Seljak et al., 2001; Springel et al., 2001; Refregier and Teyssier, 2000; Komatsu et al., 2001a). While a big uncertainty in the predictions has been lying in a phenomenological model which describes the SZ surface brightness profile of halos, Komatsu and Seljak (2001) have proposed universal gas and temperature profiles, and predicted the SZ profile relying on the physical basis. Hence, using those universal profiles, one can improve the analytic prediction for the SZ power spectrum. We expect that the universal profiles describe the SZ profile in the average sense; on the individual halo-to-halo basis, there could be significant deviation from the universal profile, owing to substructures in halos (Komatsu et al., 2001c).

4.3.2 Extragalactic radio and infrared sources

The bispectrum from extragalactic radio and infrared sources whose fluxes, F, are smaller than a certain detection threshold, $F_{\rm d}$, is simple to estimate, when we assume the Poisson distribution. Toffolatti et al. (1998) have shown that the Poisson distribution is good approximation. The Poisson distribution has the white noise spectrum; thus, the reduced bispectrum (Eq.(4.5)) is constant, $b^{\rm ps}_{l_1 l_2 l_3} = b^{\rm ps} =$ constant, and we obtain

$$B^{m_1 m_2 m_3}_{l_1 l_2 l_3} = \mathcal{G}^{m_1 m_2 m_3}_{l_l 1_2 l_3} b^{\rm ps}, \tag{4.40}$$

where

$$b^{\rm ps}(< F_{\rm d}) \equiv g^3(x) \int_0^{F_{\rm d}} dF F^3 \frac{dn}{dF} = g^3(x) \frac{n(> F_{\rm d})}{3-\beta} F_{\rm d}^3. \tag{4.41}$$

Here, dn/dF is the differential source count per unit solid angle, and $n(> F_{\rm d}) \equiv \int_{F_{\rm d}}^{\infty} dF(dn/dF)$. We have assumed a power-law count, $dn/dF \propto F^{-\beta-1}$, for $\beta < 2$. The other symbols mean $x \equiv h\nu/k_{\rm B}T \simeq (\nu/56.80\ {\rm GHz})(T/2.726\ {\rm K})^{-1}$, and

$$g(x) \equiv 2\frac{(hc)^2}{(k_{\rm B}T)^3}\left(\frac{\sinh x/2}{x^2}\right)^2 \simeq \frac{1}{67.55\ {\rm MJy\ sr}^{-1}}\left(\frac{T}{2.726\ {\rm K}}\right)^{-3}\left(\frac{\sinh x/2}{x^2}\right)^2. \tag{4.42}$$

Using the Poisson angular power spectrum, $C^{\rm ps}$, given by

$$C^{\rm ps}(< F_{\rm d}) \equiv g^2(x) \int_0^{F_{\rm d}} dF F^2 \frac{dn}{dF} = g^2(x) \frac{n(> F_{\rm d})}{2-\beta} F_{\rm d}^2, \tag{4.43}$$

we can rewrite $b^{\rm ps}$ into a different form,

$$b^{\rm ps}(< F_{\rm d}) = \frac{(2-\beta)^{3/2}}{3-\beta}\left[n(> F_{\rm d})\right]^{-1/2}\left[C^{\rm ps}(< F_{\rm d})\right]^{3/2}. \tag{4.44}$$

Toffolatti et al. (1998) have estimated $n(> F_{\rm d}) \sim 300\ {\rm sr}^{-1}$ for $F_{\rm d} \sim 0.2$ Jy at 217 GHz. This $F_{\rm d}$ corresponds to 5σ detection threshold for the *Planck* experiment at 217 GHz. Refregier et al. (2000) have extrapolated their estimation to 94 GHz, finding $n(> F_{\rm d}) \sim 7\ {\rm sr}^{-1}$ for $F_{\rm d} \sim 2$ Jy, which corresponds to *MAP* 5σ threshold. These values yield

$$C^{\rm ps}(90\ {\rm GHz}, < 2\ {\rm Jy}) \sim 2 \times 10^{-16}, \tag{4.45}$$
$$C^{\rm ps}(217\ {\rm GHz}, < 0.2\ {\rm Jy}) \sim 1 \times 10^{-17}. \tag{4.46}$$

Thus, rough estimates for $b^{\rm ps}$ are

$$b^{\rm ps}(90\ {\rm GHz}, < 2\ {\rm Jy}) \sim 2 \times 10^{-25}, \tag{4.47}$$
$$b^{\rm ps}(217\ {\rm GHz}, < 0.2\ {\rm Jy}) \sim 5 \times 10^{-28}. \tag{4.48}$$

While we have assumed the Euclidean source count ($\beta = 3/2$) for definiteness, this assumption does not affect an order of magnitude estimate here.

As the primary reduced bispectrum is $\propto l^{-4}$ (Eq.(4.23)), and the SZ–lensing reduced bispectrum is $\propto l^{-3}$ (Eq.(4.38)), the point-source bispectrum rapidly becomes to dominate the total bispectrum in small angular scales:

$$\frac{b_{lll}^{\rm primary}}{b^{\rm ps}} \sim l^{-4} \times 10^7 \left(\frac{f_{\rm NL}}{b^{\rm ps}/10^{-25}}\right), \tag{4.49}$$
$$\frac{b_{lll}^{\rm sz-lens}}{b^{\rm ps}} \sim l^{-3} \times 10^6 \left(\frac{j_\nu \overline{T}_{\rho 0} b_{\rm gas}}{b^{\rm ps}/10^{-25}}\right). \tag{4.50}$$

For example, the point sources overwhelm the SZ–lensing bispectrum measured by *MAP* at $l \gtrsim 100$.

What the SZ–lensing bispectrum and the point-source bispectrum look like? Figure 4.5 plots the primary, the SZ–lensing, and the point-source reduced bispecta for the equilateral configurations, $l \equiv l_1 = l_2 = l_3$. We have plotted $l^2(l+1)^2 b_{lll}/(2\pi)^2$. We find that these bispecra are very different from each other in shape on small angular scales. It thus suggests that we can separate these three contributions on the basis of shape difference. We study this point in the next section.

4.4 Measuring Bispectra

4.4.1 Fisher matrix

In this section, we study how well we can measure the primary bispectrum, and how well we can separate it from the secondary bispectra. Suppose that we fit the observed bispectrum, $B^{\rm obs}_{l_1l_2l_3}$, by theoretically calculated bispectra, which include both the primary and secondary sources. We minimize χ^2 defined by

$$\chi^2 \equiv \sum_{2\le l_1\le l_2\le l_3} \frac{\left(B^{\rm obs}_{l_1l_2l_3} - \sum_i A_i B^{(i)}_{l_1l_2l_3}\right)^2}{\sigma^2_{l_1l_2l_3}}, \tag{4.51}$$

where i denotes a component such as the primary, the SZ and lensing effects, extragalactic sources, and so on. We have removed unobservable modes, $l = 0$ and 1.

As we have shown in chapter 3, the variance of the bispectrum, $\sigma^2_{l_1l_2l_3}$, is the six-point function of a_{lm} (Luo, 1994; Heavens, 1998). When non-Gaussianity is weak, we calculate it as (Spergel and Goldberg, 1999; Gangui and Martin, 2000)

$$\sigma^2_{l_1l_2l_3} \equiv \left\langle B^2_{l_1l_2l_3}\right\rangle - \left\langle B_{l_1l_2l_3}\right\rangle^2 \approx \mathcal{C}_{l_1}\mathcal{C}_{l_2}\mathcal{C}_{l_3}\Delta_{l_1l_2l_3}, \tag{4.52}$$

where $\Delta_{l_1l_2l_3}$ takes values 1, 2, or 6 when all l's are different, two are same, or all are same, respectively. $\mathcal{C}_l \equiv C_l + C_l^{\rm N}$ is the total CMB angular power spectrum, which includes the power spectrum of the detector noise, $C_l^{\rm N}$. We calculate $C_l^{\rm N}$ analytically following Knox (1995) with the noise characteristics of relevant experiments. We do not include C_l from secondary sources, as they are subdominant compared with the primary C_l and $C_l^{\rm N}$ for relevant experiments. Including C_l from extragalactic sources (Eqs.(4.45) or (4.46)) changes our results less than 10%.

Taking $\partial\chi^2/\partial A_i = 0$, we obtain normal equation,

$$\sum_j \left[\sum_{2\le l_1\le l_2\le l_3} \frac{B^{(i)}_{l_1l_2l_3} B^{(j)}_{l_1l_2l_3}}{\sigma^2_{l_1l_2l_3}}\right] A_j = \sum_{2\le l_1\le l_2\le l_3} \frac{B^{\rm obs}_{l_1l_2l_3} B^{(i)}_{l_1l_2l_3}}{\sigma^2_{l_1l_2l_3}}. \tag{4.53}$$

We then define the Fisher matrix, F_{ij}, as

$$\begin{aligned} F_{ij} &\equiv \sum_{2\le l_1\le l_2\le l_3} \frac{B^{(i)}_{l_1l_2l_3} B^{(j)}_{l_1l_2l_3}}{\sigma^2_{l_1l_2l_3}} \\ &= \frac{2}{\pi} \sum_{2\le l_1\le l_2\le l_3} \left(l_1+\frac12\right)\left(l_2+\frac12\right)\left(l_3+\frac12\right) \left(\begin{array}{ccc} l_1 & l_2 & l_3 \\ 0 & 0 & 0 \end{array}\right)^2 \frac{b^{(i)}_{l_1l_2l_3} b^{(j)}_{l_1l_2l_3}}{\sigma^2_{l_1l_2l_3}}, \end{aligned} \tag{4.54}$$

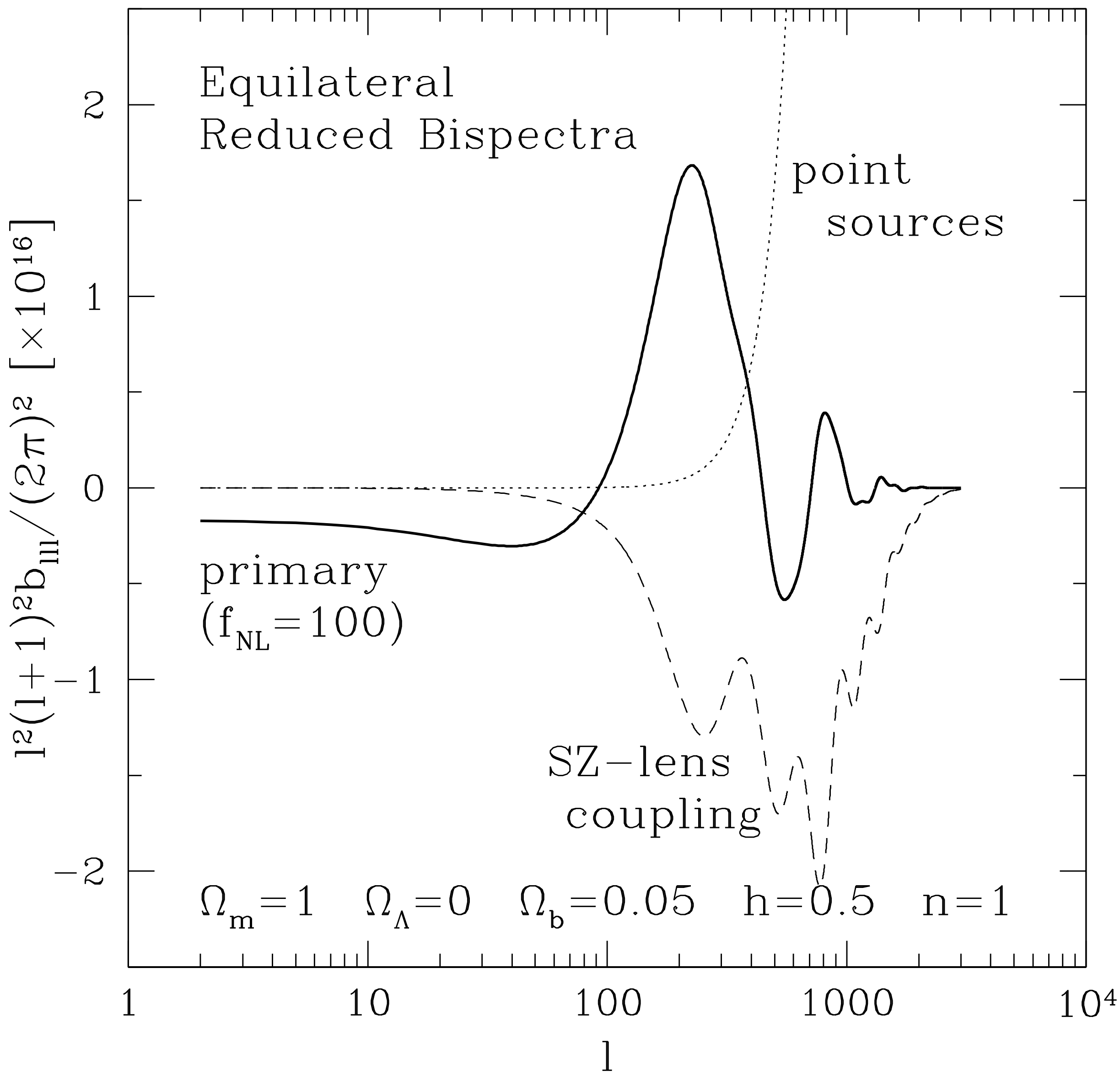

Figure 4.5: Equilateral Reduced Bispectra

Comparison between the primary (solid line), the SZ–lensing (dashed line), and the point-source (dotted line) reduced bispectra for the equilateral configurations, $l \equiv l_1 = l_2 = l_3$. We have plotted $\left[l^2(l+1)^2 b_{lll}/(2\pi)^2\right] \times 10^{16}$, which makes the Sachs–Wolfe plateau of the primary reduced bispectrum on large angular scales, $l \lesssim 10$, easily seen.

where we have used equation (4.6) to replace $B_{l_1l_2l_3}$ by the reduced bispectrum, $b_{l_1l_2l_3}$ (see Eq.(4.5) for definition). Since the covariance matrix of A_i is F_{ij}^{-1}, we define the signal-to-noise ratio, $(S/N)_i$, for a component i, the correlation coefficient, r_{ij}, between different components i and j, and the degradation parameter, d_i, of $(S/N)_i$ due to r_{ij}, as

$$\left(\frac{S}{N}\right)_i \equiv \frac{1}{\sqrt{F_{ii}^{-1}}}, \tag{4.55}$$

$$r_{ij} \equiv \frac{F_{ij}^{-1}}{\sqrt{F_{ii}^{-1}F_{jj}^{-1}}}, \tag{4.56}$$

$$d_i \equiv F_{ii}F_{ii}^{-1}. \tag{4.57}$$

Note that r_{ij} does not depend upon the amplitude of bispectra, but the shape. We have defined d_i so as $d_i = 1$ for zero degradation, while $d_i > 1$ for degraded $(S/N)_i$. Spergel and Goldberg (1999) and Cooray and Hu (2000) have considered the diagonal component of F_{ij}^{-1}. We study all the components to study the separatability between various bispectra.

We estimate an order of magnitude of S/N as a function of a certain angular resolution, l, as follows. Since the number of modes contributing to S/N increases as $l^{3/2}$, and $l^3 \begin{pmatrix} l & l & l \\ 0 & 0 & 0 \end{pmatrix}^2 \sim 0.36 \times l$, we estimate $(S/N)_i \sim (F_{ii})^{1/2}$ as

$$\left(\frac{S}{N}\right)_i \sim \frac{1}{3\pi} l^{3/2} \times l^{3/2} \left| \begin{pmatrix} l & l & l \\ 0 & 0 & 0 \end{pmatrix} \right| \times \frac{l^3 b_{lll}^{(i)}}{(l^2C_l)^{3/2}} \sim l^5 b_{lll}^{(i)} \times 4 \times 10^{12}, \tag{4.58}$$

where we have used $l^2C_l \sim 6 \times 10^{-10}$.

Table 4.1 tabulates F_{ij}, while table 4.2 tabulates F_{ij}^{-1}; table 4.3 tabulates $(S/N)_i$, while table 4.4 tabulates d_i in the diagonal, and r_{ij} in the off-diagonal parts.

4.4.2 Measuring primary bispectrum

Figure 4.6 shows the signal-to-noise ratio, S/N. The top panel shows the differential S/N for the primary bispectrum at $\ln l_3$ interval, $\left[d(S/N)^2/d\ln l_3\right]^{1/2} f_{\rm NL}^{-1}$, and the bottom panel shows the cumulative S/N, $(S/N)(< l_3)f_{\rm NL}^{-1}$, which is S/N summed up to a certain l_3. We have computed the detector noise power spectrum, $C_l^{\rm N}$, for *COBE* four-year map (Bennett et al., 1996), *MAP* 90 GHz channel, and *Planck* 217 GHz channel, and assumed full sky coverage. Figure 4.6 also shows the ideal experiment with no noise: $C_l^{\rm N} = 0$. Both $\left[d(S/N)^2/d\ln l_3\right]^{1/2}$ and $(S/N)(< l_3)$ increase monotonically with l_3, roughly $\propto l_3$, up to $l_3 \sim 2000$ for the ideal experiment.

Beyond $l_3 \sim 2000$, an enhancement of the damping tail in C_l because of the weak lensing effect (Seljak, 1996) stops $\left[d(S/N)^2/d\ln l_3\right]^{1/2}$, and hence $(S/N)(< l_3)$, increasing. This leads to an important constraint on the observation; even for the ideal noise-free, infinitesimally thin beam experiment, there is an upper limit on the value of $S/N \lesssim 0.3 f_{\rm NL}$. For a given realistic experiment, $\left[d(S/N)^2/d\ln l_3\right]^{1/2}$ has a maximum at a scale near the beam size.

Table 4.1: Fisher Matrix

Fisher matrix, F_{ij} (Eq.(4.54)). i denotes a component in the first row; j denotes a component in the first column. $\overline{T}_{\rho 0}$ is in units of 1 keV, $b_{25}^{\rm ps} \equiv b^{\rm ps}/10^{-25}$, and $b_{27}^{\rm ps} \equiv b^{\rm ps}/10^{-27}$.

COBE	primary	SZ–lensing	point sources
primary	$4.2\times10^{-6}\ f_{\rm NL}^2$	$-4.0\times10^{-7}\ f_{\rm NL} j_\nu \overline{T}_{\rho 0} b_{\rm gas}$	$-1.0\times10^{-9}\ f_{\rm NL} b_{25}^{\rm ps}$
SZ–lensing		$1.3\times10^{-7}\ (j_\nu \overline{T}_{\rho 0} b_{\rm gas})^2$	$3.1\times10^{-10}\ j_\nu \overline{T}_{\rho 0} b_{\rm gas} b_{25}^{\rm ps}$
point sources			$1.1\times10^{-12}\ (b_{25}^{\rm ps})^2$
MAP			
primary	$3.4\times10^{-3}\ f_{\rm NL}^2$	$2.6\times10^{-3}\ f_{\rm NL} j_\nu \overline{T}_{\rho 0} b_{\rm gas}$	$2.4\times10^{-3}\ f_{\rm NL} b_{25}^{\rm ps}$
SZ–lensing		$0.14\ (j_\nu \overline{T}_{\rho 0} b_{\rm gas})^2$	$0.31\ j_\nu \overline{T}_{\rho 0} b_{\rm gas} b_{25}^{\rm ps}$
point sources			$5.6\ (b_{25}^{\rm ps})^2$
Planck			
primary	$3.8\times10^{-2}\ f_{\rm NL}^2$	$7.2\times10^{-2}\ f_{\rm NL} j_\nu \overline{T}_{\rho 0} b_{\rm gas}$	$1.6\times10^{-2}\ f_{\rm NL} b_{27}^{\rm ps}$
SZ–lensing		$39\ (j_\nu \overline{T}_{\rho 0} b_{\rm gas})^2$	$5.7\ j_\nu \overline{T}_{\rho 0} b_{\rm gas} b_{27}^{\rm ps}$
point sources			$2.7\times10^{3}\ (b_{27}^{\rm ps})^2$

Table 4.2: Inverted Fisher Matrix

Inverted Fisher matrix, F_{ij}^{-1}. The meaning of the symbols is the same as in table 4.1.

COBE	primary	SZ–lensing	point sources
primary	$3.5\times10^{5}\ f_{\rm NL}^{-2}$	$1.1\times10^{6}\ (f_{\rm NL} j_\nu \overline{T}_{\rho 0} b_{\rm gas})^{-1}$	$1.3\times10^{7}\ (f_{\rm NL} b_{25}^{\rm ps})^{-1}$
SZ–lensing		$3.1\times10^{7}\ (j_\nu \overline{T}_{\rho 0} b_{\rm gas})^{-2}$	$-7.8\times10^{9}\ (j_\nu \overline{T}_{\rho 0} b_{\rm gas} b_{25}^{\rm ps})^{-1}$
point sources			$3.1\times10^{12}\ (b_{25}^{\rm ps})^{-2}$
MAP			
primary	$3.0\times10^{2}\ f_{\rm NL}^{-2}$	$-6.1\ (f_{\rm NL} j_\nu \overline{T}_{\rho 0} b_{\rm gas})^{-1}$	$0.21\ (f_{\rm NL} b_{25}^{\rm ps})^{-1}$
SZ–lensing		$8.4\ (j_\nu \overline{T}_{\rho 0} b_{\rm gas})^{-2}$	$-0.46\ (j_\nu \overline{T}_{\rho 0} b_{\rm gas} b_{25}^{\rm ps})^{-1}$
point sources			$0.21\ (b_{25}^{\rm ps})^{-2}$
Planck			
primary	$26\ f_{\rm NL}^{-2}$	$-4.9\times10^{-2}\ (f_{\rm NL} j_\nu \overline{T}_{\rho 0} b_{\rm gas})^{-1}$	$-5.7\times10^{-5}\ (f_{\rm NL} b_{27}^{\rm ps})^{-1}$
SZ–lensing		$2.6\times10^{-2}\ (j_\nu \overline{T}_{\rho 0} b_{\rm gas})^{-2}$	$-5.4\times10^{-5}\ (j_\nu \overline{T}_{\rho 0} b_{\rm gas} b_{27}^{\rm ps})^{-1}$
point sources			$3.7\times10^{-4}\ (b_{27}^{\rm ps})^{-2}$

Table 4.3: Signal-to-noise Ratio

Signal-to-noise ratio, $(S/N)_i$ (Eq.(4.55)), of detecting the bispectrum. i denotes a component in the first row. The meaning of the symbols is the same as in table 4.1.

	primary	SZ–lensing	point sources
COBE	$1.7 \times 10^{-3}\ f_{\rm NL}$	$1.8 \times 10^{-4}\ \lvert j_\nu \rvert \overline{T}_{\rho 0} b_{\rm gas}$	$5.7 \times 10^{-7}\ b_{25}^{\rm ps}$
MAP	$5.8 \times 10^{-2}\ f_{\rm NL}$	$0.34\ \lvert j_\nu \rvert \overline{T}_{\rho 0} b_{\rm gas}$	$2.2\ b_{25}^{\rm ps}$
Planck	$0.19\ f_{\rm NL}$	$6.2\ \lvert j_\nu \rvert \overline{T}_{\rho 0} b_{\rm gas}$	$52\ b_{27}^{\rm ps}$

Table 4.4: Signal Degradation and Correlation Matrix

Signal degradation parameter, d_i (Eq.(4.57)), and correlation coefficient, r_{ij} (Eq.(4.56)), matrix. i denotes a component in the first row; j denotes a component in the first column. d_i for $i = j$, while r_{ij} for $i \neq j$.

COBE	primary	SZ–lensing	point sources
primary	1.46	$0.33\ {\rm sgn}(j_\nu)$	1.6×10^{-2}
SZ–lensing		3.89	$-0.79\ {\rm sgn}(j_\nu)$
point sources			3.45
MAP			
primary	1.01	$-0.12\ {\rm sgn}(j_\nu)$	2.7×10^{-2}
SZ–lensing		1.16	$-0.35\ {\rm sgn}(j_\nu)$
point sources			1.14
Planck			
primary	1.00	$-5.9 \times 10^{-2}\ {\rm sgn}(j_\nu)$	-5.8×10^{-4}
SZ–lensing		1.00	$-1.8 \times 10^{-2}\ {\rm sgn}(j_\nu)$
point sources			1.00

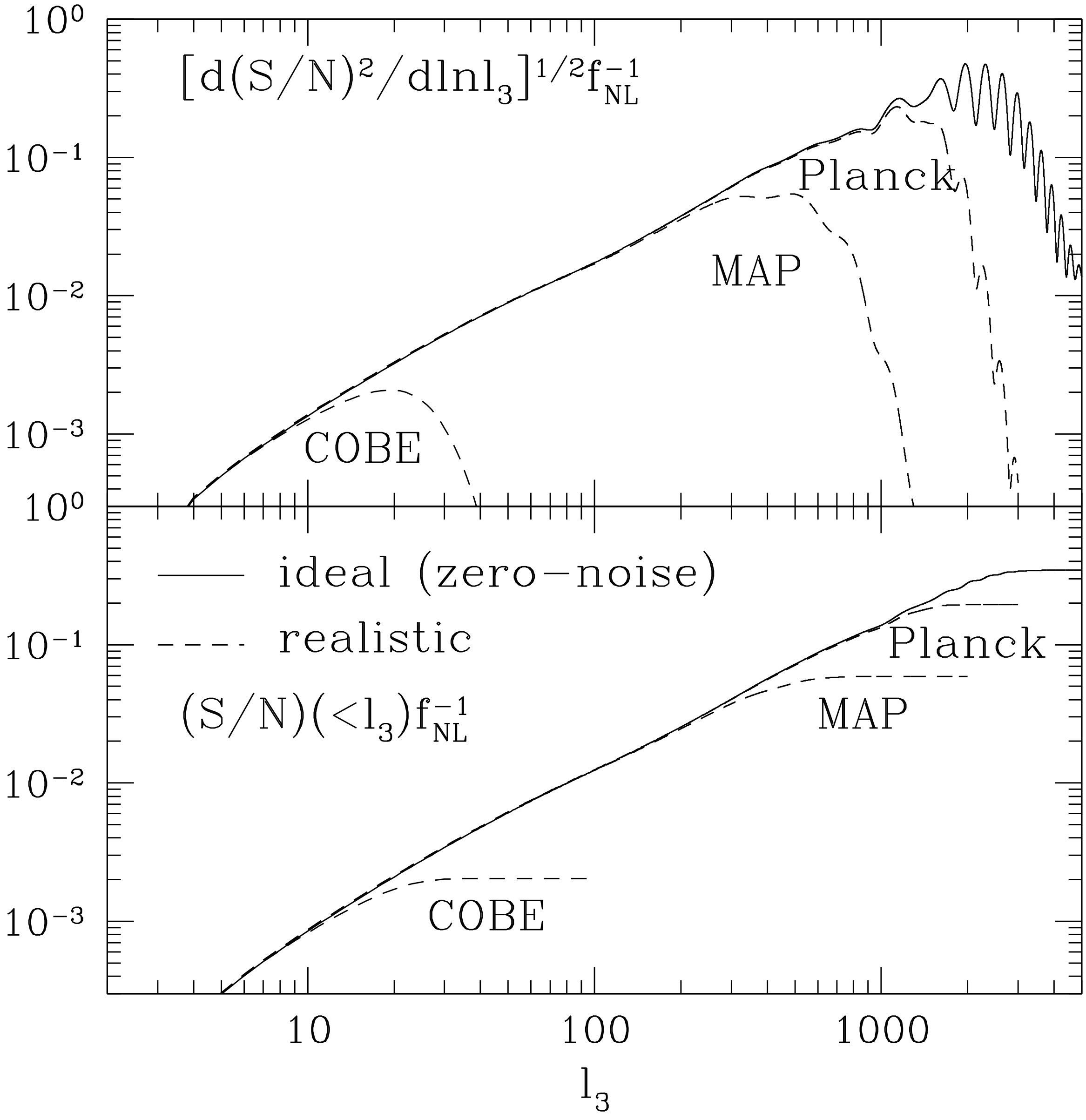

Figure 4.6: Signal-to-noise Ratio

The predictions of the signal-to-noise ratio, S/N, for *COBE*, *MAP*, and *Planck* experiments (see Eq.(4.55)). The differential S/N at $\ln l_3$ interval is shown in the upper panel, while the cumulative S/N up to a certain l_3 is shown in the bottom panel. Both are in units of $f_{\rm NL}$. Solid line represents the zero-noise ideal experiment, while dotted lines show the realistic experiments mentioned above. The total $(S/N)f_{\rm NL}^{-1}$ are 1.7×10^{-3}, 5.8×10^{-2}, and 0.19 for *COBE*, *MAP*, and *Planck* experiments, respectively.

For *COBE*, *MAP* and *Planck* experiments, the total $(S/N)f_{\rm NL}^{-1}$ are 1.7×10^{-3}, 5.8×10^{-2}, and 0.19, respectively (see table 4.3). To obtain $S/N>1$, we need $f_{\rm NL}>600$, 20, and 5, while the ideal experiment requires $f_{\rm NL}>3$ (see table 4.5). We can also roughly obtain these values by substituting equation (4.23) into (4.58),

$$\left(\frac{S}{N}\right)_{\rm primary}\sim l\times10^{-4}f_{\rm NL}. \tag{4.59}$$

The degradation parameters, $d_{\rm primary}$, are 1.46, 1.01, and 1.00 for *COBE*, *MAP*, and *Planck* experiments, respectively (see table 4.4), suggesting that *MAP* and *Planck* experiments will separate the primary bispectrum from the others with 1% or better accuracy; however, *COBE* cannot discriminate between them very well, as the primary and the secondary sources change monotonically on the *COBE* angular scales. On the *MAP* and *Planck* scales, the primary bispectrum starts oscillating around zero, being well separated in shape from the secondaries that do not oscillate. This is good news for the forthcoming high angular resolution CMB experiments.

4.4.3 Measuring secondary bispectra

Signal-to-noise ratios of detecting the SZ–lensing bispectrum, $(S/N)_{\rm sz-lens}$, in units of $|j_\nu|\,\overline{T}_{\rho0}b_{\rm gas}$ are 1.8×10^{-4}, 0.34, and 6.2 for *COBE*, *MAP*, and *Planck* experiments, respectively (see table 4.3), where $\overline{T}_{\rho0}$ is in units of 1 keV. Using equations (4.58) and (4.38), we estimate $(S/N)_{\rm sz-lens}$ roughly as

$$\left(\frac{S}{N}\right)_{\rm sz-lens}\sim l^2\times10^{-6}\,|j_\nu|\,\overline{T}_{\rho0}b_{\rm gas}. \tag{4.60}$$

Hence, $(S/N)_{\rm sz-lens}$ increases with the angular resolution more rapidly than the primary bispectrum (see Eq.(4.59)). Since $|j_\nu|\,\overline{T}_{\rho0}b_{\rm gas}$ should be of order unity, *COBE* and *MAP* cannot detect the SZ–lensing bispectrum; however, *Planck* is sensitive enough to detect, depending on the frequency, i.e., a value of j_ν. For example, 217 GHz is insensitive to the SZ effect as $j_\nu\sim0$, while $j_\nu=-2$ in the Rayleigh–Jeans regime.

The degradation parameters, $d_{\rm sz-lens}$, are 3.89, 1.16, and 1.00 for *COBE*, *MAP*, and *Planck* experiments, respectively (see table 4.4); thus, *Planck* will separate the SZ–lensing bispectrum from the other effects. Note that $(S/N)_{\rm sz-lens}$ values must be an order of magnitude estimation, for our cosmological model is the *COBE* normalized SCDM that yields $\sigma_8=1.2$, which is a factor of 2 greater than the cluster normalization for $\Omega_{\rm m}=1$, and 20% greater than the normalization for $\Omega_{\rm m}=0.3$ (Kitayama and Suto, 1997). Hence, this factor tends to overestimate $\left\langle\Theta_{lm}^*a_{lm}^{\rm SZ}\right\rangle$ (Eq.(4.37)) by a factor of less than 10; on the other hand, using the linear $P_\Phi(k)$ power spectrum rather than the non-linear power spectrum tends to underestimate the effect by a factor of less than 10 at $l\sim3000$ (Cooray and Hu, 2000). Yet, our main goal is to discriminate between the shapes of various bispectra, not to determine the amplitude, so that this factor does not affect our conclusion on the degradation parameters, d_i.

For the extragalactic radio and infrared sources, we estimate the signal-to-noise ratios as $5.7\times10^{-7}(b^{\rm ps}/10^{-25})$, $2.2(b^{\rm ps}/10^{-25})$, and $52(b^{\rm ps}/10^{-27})$ for *COBE*, *MAP*, and *Planck* experiments, respectively (see table 4.3), and the degradation parameters, $d_{\rm ps}$, as 3.45, 1.14, and 1.00

(see table 4.4). Our estimate is consistent with Refregier et al. (2000). From equation (4.58), we find

$$\left(\frac{S}{N}\right)_{\rm ps} \sim l^5 \times 10^{-13} \left(\frac{b^{\rm ps}}{10^{-25}}\right); \tag{4.61}$$

thus, S/N of the point-source bispectrum increases very rapidly with the angular resolution.

Although *MAP* cannot separate the Poisson bispectrum from the SZ–lensing bispectrum very well (see r_{ij} in table 4.4), the SZ–lensing bispectrum is too small to be measured by *MAP* anyway. *Planck* will do an excellent job on separating all kinds of bispectra, at least including the primary signal, SZ–lensing coupling, and extragalactic point sources, on the basis of the shape difference.

4.4.4 Measuring primary skewness

For the skewness, we define S/N as

$$\left(\frac{S}{N}\right)^2 \equiv \frac{S_3^2}{\sigma_{S_3}^2}, \tag{4.62}$$

where the variance is (Srednicki, 1993)

$$\begin{aligned}
\sigma_{S_3}^2 &\equiv \left\langle (S_3)^2 \right\rangle = 6\int_{-1}^{1} \frac{d\cos\theta}{2} \left[\mathcal{C}(\theta)\right]^3 \\
&= 6\sum_{l_1 l_2 l_3} \frac{(2l_1+1)(2l_2+1)(2l_3+1)}{(4\pi)^3} \left(\begin{array}{ccc} l_1 & l_2 & l_3 \\ 0 & 0 & 0 \end{array}\right)^2 \mathcal{C}_{l_1}\mathcal{C}_{l_2}\mathcal{C}_{l_3} W_{l_1}^2 W_{l_2}^2 W_{l_3}^2 \\
&= \frac{9}{2\pi^3} \sum_{2\le l_1 \le l_2 \le l_3} \left(l_1+\frac{1}{2}\right)\left(l_2+\frac{1}{2}\right)\left(l_3+\frac{1}{2}\right) \left(\begin{array}{ccc} l_1 & l_2 & l_3 \\ 0 & 0 & 0 \end{array}\right)^2 \\
&\quad \times \mathcal{C}_{l_1}\mathcal{C}_{l_2}\mathcal{C}_{l_3} W_{l_1}^2 W_{l_2}^2 W_{l_3}^2.
\end{aligned} \tag{4.63}$$

In the last equality, we have used symmetry of the summed quantity with respect to indices (Eq.(4.29)), and removed unobservable modes, $l = 0$ and 1. Typically $\sigma_{S_3} \sim 10^{-15}$, as $\sigma_{S_3} \sim [\mathcal{C}(0)]^{3/2} \sim 10^{-15}$, where $\mathcal{C}(\theta)$ is the temperature auto correlation function including noise.

The bottom panel of figure 4.3 plots $\sigma_{S_3}(< l_3)$, which is σ_{S_3} summed up to a certain l_3, for *COBE*, *MAP*, and *Planck* experiments as well as for the ideal experiment. Since $\mathcal{C}_l W_l^2 = \mathcal{C}_l e^{-l(l+1)\sigma_{\rm b}^2} + w^{-1}$, where w^{-1} is the white noise power spectrum of the detector noise (Knox, 1995), w^{-1} keeps $\sigma_{S_3}(< l_3)$ slightly increasing with l_3 beyond the experimental angular resolution scale, $l \sim \sigma_{\rm b}^{-1}$. In contrast, $S_3(< l_3)$ becomes constant beyond $l \sim \sigma_{\rm b}^{-1}$ (see the top panel of figure 4.3). As a result, S/N starts slightly decreasing beyond the resolution. We use the maximum S/N for calculating the minimum value of $f_{\rm NL}$ above which the primary S_3 is detectable; we find that $f_{\rm NL} > 800$, 80, 70, and 60 for *COBE*, *MAP*, *Planck*, and the ideal experiments, respectively, assuming full sky coverage.

These $f_{\rm NL}$ values are systematically larger than those for detecting $B_{l_1 l_2 l_3}$ by a factor of 1.3, 4, 14, and 20, respectively (see table 4.5). The higher the angular resolution is, the less sensitive the primary S_3 is to non-Gaussianity than $B_{l_1 l_2 l_3}$. This is because the cancellation effect on smaller angular scales because of the oscillation of $B_{l_1 l_2 l_3}$ damps S_3.

Table 4.5: Detection Limit for the Non-linear Coupling Parameter

The minimum non-linear coupling parameter, $f_{\rm NL}$, needed for detecting the primary non-Gaussianity by the bispectrum or the skewness with the signal-to-noise ratio greater than 1. These estimates include the effects of cosmic variance, detector noise, and foreground sources.

Experiments	$f_{\rm NL}$ (Bispectrum)	$f_{\rm NL}$ (Skewness)
COBE	600	800
MAP	20	80
Planck	5	70
Ideal	3	60

4.5 Discussion and Conclusions

In this chapter, using the full radiation transfer function, we have numerically computed the primary cosmic microwave background bispectrum (Eq.(4.19)) and skewness (Eq.(4.28)) down to arcminutes angular scales. As the primary bispectrum oscillates around zero (figure 4.2), the primary skewness saturates at the *MAP* angular resolution scale, $l \sim 500$ (figure 4.3). We have introduced the *reduced* bispectrum, $b_{l_1 l_2 l_3}$, defined by equation (4.5), and found that this quantity is more useful to describe physical properties of the bispectrum than the angular averaged bispectrum, $B_{l_1 l_2 l_3}$ (Eq.(4.3)).

Figure 4.7 compares the expected signal-to-noise ratio of detecting the primary non-Gaussianity based on the bispectrum (Eq.(4.55)) with that based on the skewness (Eq.(4.62)). It shows that the bispectrum is almost an order of magnitude more sensitive to the non-Gaussianity than the skewness. We conclude that when we can compute the predicted form of the bispectrum, it becomes a "matched filter" for detecting the non-Gaussianity in data, and thus much more powerful tool than the skewness. Table 4.5 summarizes the minimum $f_{\rm NL}$ for detecting the primary non-Gaussianity using the bispectrum or the skewness for *COBE*, *MAP*, *Planck*, and the ideal experiments. This shows that even the ideal experiment needs $f_{\rm NL} > 3$ to detect the primary bispectrum.

We have calculated the secondary bispectra from the coupling between the SZ effect and the weak lensing effect, and from the extragalactic radio and infrared sources. Only *Planck* will detect the SZ–lensing bispectrum, while both *MAP* and *Planck* will detect the extragalactic point-source bispectrum (table 4.3).

We have also studied how well we can discriminate between the primary, the SZ–lensing coupling, and the extragalactic point-source bispectra. We have found that *MAP* and *Planck* will separate the primary from the other secondary sources with 1% or better accuracy. This conclusion is due to the acoustic oscillation in the primary bispectrum that does not appear in the secondary bispectra. The SZ–lensing coupling and the extragalactic sources are well separately measured by *Planck* experiment, although *COBE* and *MAP* cannot discriminate between them (table 4.4).

Our arguments on the ability to discriminate between various bispectra have been based upon

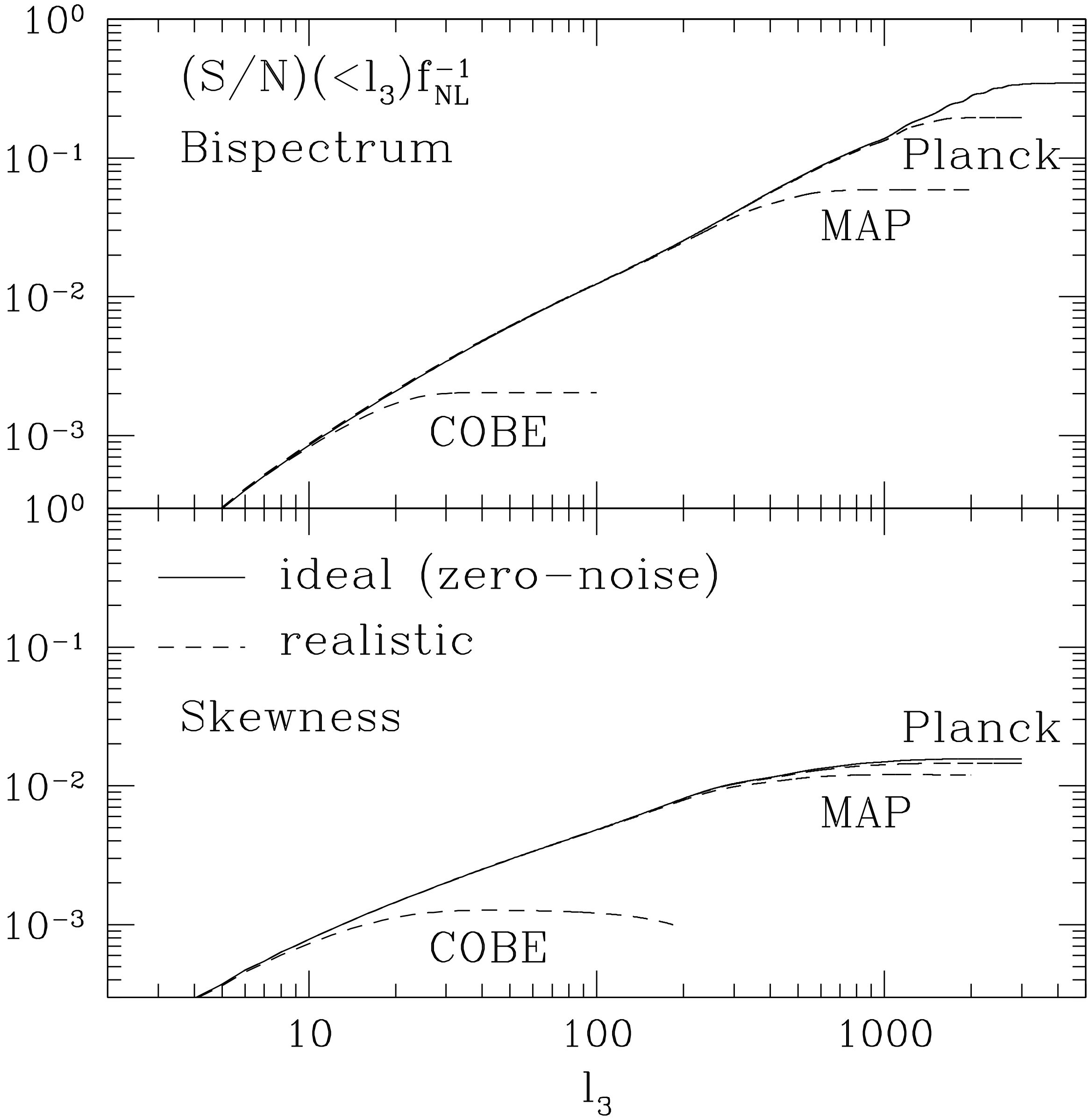

Figure 4.7: Bispectrum vs Skewness

Comparison of the signal-to-noise ratio summed up to a certain l_3, $S/N(< l_3)$, for the bispectrum (top panel; Eq.(4.55)) and the skewness (bottom panel; Eq.(4.62)). $S/N(< l_3)$ is in units of $f_{\rm NL}$. The dotted lines show *COBE*, *MAP*, and *Planck* experiments (dotted lines), while the solid line shows the ideal experiment. See table 4.5 for $f_{\rm NL}$ to obtain $S/N > 1$.

the shape difference, and thus have not taken into account the spectral difference in frequency space. Tegmark and Efstathiou (1996) and Cooray et al. (2000) have shown that the multi-band observation is efficient for discriminating between the primary signal and the other foreground sources in the CMB power spectrum. Their scheme should be effective on the bispectrum as well, and will improve the accuracy of the foreground removal further. We thus expect that *MAP* and *Planck* will measure the primary bispectrum separately from the foregrounds.

Simple slowly-rolling single-field inflation models predict $f_{\rm NL} \sim \mathcal{O}(10^{-2})$ (Salopek and Bond, 1990, 1991; Gangui et al., 1994), while the second order perturbation theory predicts $f_{\rm NL} \sim \mathcal{O}(1)$ (Pyne and Carroll, 1996); thus, significant detection of the primary bispectrum or the skewness with any experiments means that these inflation models need to be modified. According to our results, if the reported detection (Ferreira et al., 1998; Magueijo, 2000) of the bispectrum on the *COBE* map were cosmological in origin, then *MAP* and *Planck* would detect the primary bispectrum much more significantly. While Banday, Zaroubi and Górski (Banday et al., 2000) have shown that the one of those detections (Ferreira et al., 1998) is accounted for by the experimental systematic effects, the other (Magueijo, 2000) is significant even after removing such the systematics.

Although we have not discussed so far, spatial distribution of interstellar dust emissions is a potential source of microwave non-Gaussianity. While it is very hard to estimate the bispectrum analytically, we can use the dust template map compiled by Schlegel et al. (1998) to estimate the dust bispectrum. For example, we have found that the dimensionless skewness parameter, $\left\langle (\Delta T)^3 \right\rangle / \left\langle (\Delta T)^2 \right\rangle^{3/2}$, is as large as 51 on the template map. We have used the publicly available HEALPix-formatted (Górski et al., 1998) 100 μm map, which contains 12,582,912 pixels without sky-cut. The mean intensity in the map is 14.8 MJy sr^{-1}. Of course, this skewness is largely an overestimate for the real CMB measurement; we need to cut a fraction of the sky that contains the Galactic plane, and this will greatly reduce the non-Gaussianity. Nevertheless, residual non-Gaussianity is still a source of the microwave bispectrum, and has to be taken into account. Moreover, the form of the measured bispectrum on the dust map reflects the physics of interstellar dust, which is highly uncertain at present; thus, studying the interstellar dust bispectrum is a challenging field.